NIH Public Access
Author Manuscript
Magn Reson Med. Author manuscript; available in PMC 2010 August 1.

Published in final edited form as:
Magn Reson Med. 2009 August ; 62(2): 384–393. doi:10.1002/mrm.21980.

Direct Saturation MRI: Theory and Application to Imaging Brain Iron

Seth A. Smith[1,2], **Jeff W.M. Bulte**[1,3,4,5], and **Peter C. M. van Zijl**[1,2,†]

[1]Russell H. Morgan Department of Radiology and Radiological Science, Johns Hopkins University School of Medicine, Baltimore, MD

[2]F.M. Kirby Research Center for Functional Brain Imaging Kennedy Krieger Institute, Baltimore, MD

[3]Department of Biomedical Engineering, The Johns Hopkins University School of Medicine, Baltimore, MD

[4]Department of Chemical & Biomolecular Engineering, The Johns Hopkins University Whiting School of Engineering

[5]Cellular Imaging Section and Vascular Biology Program, Institute for Cellular Engineering, Johns Hopkins University School of Medicine, Baltimore, MD

Abstract

When applying RF saturation to tissue, MRI signal reductions occur due to magnetization transfer (MT) and direct saturation (DS) effects on water protons. It is shown that the direct effects, often considered a nuisance, can be used to distinguish gray matter regions with different iron content. Direct saturation effects were selected by reducing the magnitude and duration of RF irradiation to minimize confounding MT effects. Contrary to MT saturation spectra, direct water saturation spectra are characterized by a symmetric Lorentzian-shaped frequency dependence that can be described by an exact analytical solution of the Bloch equations. The effect of increased transverse relaxation, e.g. due to the presence of iron, will broaden this saturation spectrum. As a first application, direct saturation ratio (DSR) images were acquired to visualize gray matter structures in the human brain. Similar to T_2*w images, the quality of DSR images was affected by local field inhomogeneity, but this could be easily corrected for by centering the saturation spectrum on a voxel-by-voxel basis. The results show that, contrary to commonly used T_2*-weighted and absolute R_2 images, the DSR images visualize all gray matter structures, including cortex. A direct correlation between DSR and iron content was confirmed for these structures.

Keywords

Magnetization Transfer; Direct Saturation; brain iron; transverse relaxation

Introduction

Recently, when performing high resolution magnetization transfer (MT) measurements of the brain at 3T, we noticed statistically significant differences between the MT ratios (MTR) in different gray matter (GM) regions (1). These GM structures are known to have different levels of iron concentration (2), suggesting the potential for MT images to report on iron

† Author for Correspondence, Peter C.M. van Zijl, Johns Hopkins University School of Medicine, Dept. of Radiology, 217 Traylor Bldg, 720 Rutland Ave, Baltimore, MD, 21205, pvanzijl@mri.jhu.edu, Tel: 443-923-9500, Fax: 443-923-9511.

NIH-PA Author Manuscript
NIH-PA Author Manuscript
NIH-PA Author Manuscript

NIH-PA Author Manuscript

NIH-PA Author Manuscript

NIH-PA Author Manuscript

content. Several earlier reports in the literature also suggest that the presence of iron in tissue affects the MTR, both for cerebral GM (3) and cardiac muscle (4). Interestingly, however, these reports indicated that the MTR decreases with increasing iron content. A comprehensive follow-up investigation of ferritin solutions in both agarose and polyacrylamide gels (5) confirmed the existence of this effect, but in contrast, showed that the apparent decrease in the MTR resulted from changes in the longitudinal relaxation time T_1 caused by the ferritin rather than an MT effect. The suggestion therefore was that MTR measurements performed in isolated tissue could be used to assess presence of iron if the MT effect caused by the prevalence of myelin and neuronal density in nervous system tissue could be minimized.

In an independent experiment, Zurkiya and Hu recently demonstrated that the magnitude of off-resonance RF saturation (ORS) effects increased proportionally to iron concentration in phantoms doped with superparamagnetic iron oxide (SPIO) particles (6). These results confirmed that the effect of the presence of iron on saturation experiments was distinct from MT effects and suggested an alternative explanation in terms of diffusion through magnetic field gradients. In this study, we test the hypothesis that the observed association between increased MTR and iron concentration in GM is actually due to direct water saturation, which is affected by iron concentration through a decrease in the transverse relaxation time T_2. The presumption is that a decrease in T_2 will yield a broader saturation lineshape and thus bloat the observed MTR signal. If this is true, a direct measurement of the pure water saturation line shape should directly reflect the effect of accumulation of endogenous paramagnetic metals in the human brain. However, specific measurements of the direct saturation effect are confounded by simultaneously occurring MT effects. Fortunately, reducing the power and duration of the selective RF irradiation can mitigate the MT contribution (7). When the MT effect is minimized, the remaining saturation spectrum will reflect a direct saturation lineshape, which is largely affected by T_2 as described by the exact solution of the Bloch equations during RF saturation (8).

To test this hypothesis, we measured direct saturation (DS) spectra, i.e. the magnitude of RF saturation as a function of offset frequency with respect to water, in different GM structures in the human brain. Analogously to the MTR (9-11), a direct saturation ratio (DSR)

$$DSR(\omega)=1-\frac{S(\omega)}{S_o} \quad [1]$$

was defined as the ratio of the water signal with, $S(\omega)$, and without, S_o, RF irradiation at offset frequency, ω. The results show that the DSR is directly proportional to the estimated, age-adjusted non-heme iron concentration (2) of the iron-laden GM structures in the human brain. When using the measured T_2, reported T_1 (12), and experimental B_1 amplitude and duration (t_{sat}) in these regions to predict the direct saturation curves, excellent agreement was found between the predicted and the experimentally measured direct saturation effects.

Materials and Methods

Theory

The Bloch Equations for RF irradiation in the absence of an MT effect can be written as (8):

NIH-PA Author Manuscript

NIH-PA Author Manuscript

NIH-PA Author Manuscript

$$\begin{aligned}\frac{dM_x}{dt} &= \Delta\omega M_y(t) - R_2 M_x(t)\\ \frac{dM_y}{dt} &= -\Delta\omega M_x(t) - R_2 M_y(t) + \omega_1 M_z(t)\\ \frac{dM_z}{dt} &= -\omega_1 M_y(t) - (M_z(t) - M_z^o) R_1\end{aligned} \quad [2]$$

where $M_{x,y,z}$ denotes the magnetization along x, y, z, respectively, and ω_1 the amplitude of the RF irradiation played out at $\Delta\omega = \omega_o - \omega$, the offset frequency of irradiation with respect to the water proton Larmor frequency (ω_o); $R_1 = 1/T_1$ and $R_2 = 1/T_2$. We use the rate notation in the equations and theory for brevity, but the time notation in the text for convenience of the readers who may be more familiar with relaxation time values. The analytical solution for the time-dependent signal intensity of the longitudinal magnetization, $M_z(t)$ for the case of constant RF irradiation has been given by Mulkern and Williams (8):

$$M_z(t) = m_z^{ss} + m_1 e^{\alpha_1 t} + m_2 e^{\alpha_2 t} + m_3 e^{\alpha_3 t} \quad [3]$$

in which the steady state magnetization, m_z^{ss}, is a function of R_1, R_2, $\Delta\omega$ and ω_1:

$$m_z^{ss} = \frac{m_z^{eq} R_1 [R_2^2 + (\Delta\omega)^2]}{R_1 [R_2^2 + (\Delta\omega)^2] + \omega_1^2 R_2} \quad [4]$$

and m_z^{eq} is the equilibrium magnetization in the absence of RF irradiation (herein assumed to be unity). Following Mulkern and Williams (8), the time-invariant coefficients and exponential terms of Eq. 3 are:

$$\begin{aligned}m_{1,2} &= \frac{\left[(R_2 + \alpha_{1,2})^2 + (\Delta\omega)^2\right]\left(m_z^{eq} R_1 + m_z^o \alpha_{1,2}\right) - \omega_1 \alpha_{1,2}\left[m_y^o (R_2 + \alpha_{1,2}) - (\Delta\omega) m_x^o\right]}{\alpha_{1,2}(\alpha_{1,2} - \alpha_{2,1})(\alpha_{1,2} - \alpha_3)}\\ m_3 &= m_2^*\end{aligned} \quad [5]$$

where $m_{x,y,z}^o$ are the initial conditions for the magnetizations along x, y, z, respectively, and m_3 is the complex conjugate of m_2. Assuming $m_x^o = m_y^o = 0$, and $m_z^o = m_z^{eq} = 1$, Eq. 5 simplifies to:

$$\begin{aligned}m_{1,2} &= \frac{\left[(R_2 + \alpha_{1,2})^2 + (\Delta\omega)^2\right](R_1 + \alpha_{1,2})}{\alpha_{1,2}(\alpha_{1,2} - \alpha_{2,1})(\alpha_{1,2} - \alpha_3)}\\ m_3 &= m_2^*\end{aligned} \quad [5a]$$

The exponential coefficients, α_1, α_2, α_3, are the roots to the denominator of the Laplace transforms of M_x, M_y, and M_z and are functions of the tissue parameters (R_1, R_2), and experimental parameter settings ($\Delta\omega$, ω_1):

NIH-PA Author Manuscript

NIH-PA Author Manuscript

NIH-PA Author Manuscript

$$\alpha_1=\frac{-(2R_2+R_1)}{3}+A+B$$
$$\alpha_2=\frac{-(2R_2+R_1)}{3}-\frac{(A+B)}{2}+i\sqrt{3}\frac{(A-B)}{2}$$
$$\alpha_3=\alpha_2^* \quad [6]$$

in which

$$A=\left[-\frac{b}{2}+\sqrt{c}\right]^{1/3},\ B=\left[-\frac{b}{2}-\sqrt{c}\right]^{1/3}$$
$$b=\frac{1}{27}(R_1-R_2)\left[2(R_1-R_2)^2+18(\Delta\omega)^2-9\omega_1^2\right]$$
$$c=\frac{1}{27}\left\{\left[(\Delta\omega)^2+\omega_1^2\right]^3+(R_1-R_2)^2\left(2(\Delta\omega)^2\left[2(\Delta\omega)^2+(R_1-R_2)^2\right]-\omega_1^2\left[\frac{\omega_1^2}{4}+5(\Delta\omega)^2\right]\right)\right\} \quad [7]$$

Finally, for a given saturation pulse duration ($t = t_{sat}$), the direct saturation ratio (DSR, Eq. 1) in terms of magnetization is defined as:

$$DSR(\omega)=1-\frac{M_z(t=t_{sat},\Delta\omega,\omega_1,R_1,R_2)}{M_o} \quad [8]$$

To sensitively detect changes in the direct saturation spectrum, it is necessary to minimize confounding MT effects. In theory, the optimal approach would be by choosing t_{sat} to be short and B_1 to be as low as possible. However, in practice, a minimal power is needed for sample penetration and the saturation curve needs to be sampled in sufficient detail in all voxels in the brain or other tissue of interest. If the curve is narrow, this becomes problematic if there are large differences in water frequency between different tissue regions, as will occur due to the presence of susceptibility differences between these regions (7). We therefore decided to employ a slightly longer low-amplitude pulse with some remaining MT effect.

In order to find the frequency where T_2 effects on DSR will be most pronounced, in theory, one can numerically evaluate the gradient of the difference of simulated DSR values at two different T_2's with respect to the offset frequency and evaluate the point at which the derivative is zero. However, in practice, such a value needs to be optimized with respect to the contrast to noise for a particular DSR value and therefore we determined the frequency that was most sensitive to disparate T_2 values by analyzing the range of absolute DSR differences and using the offset with the highest DSR difference and largest SNR.

Simulations

Two simulations were performed to estimate the optimal sequence parameters for DSR imaging of structures with different T_2 values. To judge the effect of power and pulse length on the saturation spectrum, we simulated Eq. 8 as a function of B_1 (0.8-4mT) using the full Bloch Equations with and without MT in a similar fashion as presented in (1) over a frequency offset range from -750 – 750 Hz and with an input of 3T GM relaxation times: T_2 = 70ms T_1 = 1100ms (13). Parameters for the simulations including the MT contribution for the semisolid component in GM were: k = 4 Hz, f = 7.5%, T_1^b = 1.2 s, T_2^b = 11 ms (14,15) where k is the rate of exchange between bound and free protons, f the size of the bound spin pool, and T_1^b, T_2^b the longitudinal and transverse relaxation times of the bound spins, respectively. The DSR Simulations using the full Bloch equations and the exact analytical solution (Eqs. 3-8) were compared. After determining the range of powers and pulse lengths

NIH-PA Author Manuscript

NIH-PA Author Manuscript

NIH-PA Author Manuscript

suitable for having saturation images that are sufficiently selective and dominated by direct saturation, we simulated the effect of transverse relaxation on the theoretical curve and determined the offset frequency for saturation at 3T most sensitive to change in T_2.

Human studies

After local institutional review board approval, 5 healthy volunteers (age range = 22 – 40 years) provided signed informed consent and underwent brain MRI. All experiments were performed on a 3.0T MR scanner (Philips Medical Systems, Best, The Netherlands) using body coil excitation and a 6-channel phased-array coil with sensitivity encoding (SENSE) for reception. For all scans, in order to minimize the effects of susceptibility differences near the sinuses on image quality, 2nd order shimming was applied over the entire imaging volume.

In order to compare DSR imaging with conventional imaging, absolute T_2 and T_2*-weighted scans were acquired. Double-echo fast spin echo sequences were obtained over the entire brain for calculation of absolute R_2 ($R_2 = 1/T_2$). The nominal (i.e. acquired) resolution was $1.2 \times 1.2 \times 2.2$ mm^3 covering 20 slices from the centrum semiovale to the medulla. Other parameters were: SENSE factor 2, Turbo factor = 23, $TR/TE_1/TE_2$ = 2500ms/30ms/80ms. T_2*-weighted images (16) were obtained using a multi-slice gradient echo technique. Nominal resolution was $1.2 \times 1.2 \times 2.2$ mm^3 covering the same FOV as the T_2 acquisition, $TR/TE/\alpha$ = 575ms/30ms/20°, SENSE factor = 2. No echo planar or turbo gradient echo imaging was employed for these conventional sequences.

DSR experiments were obtained in 10-slice axial volumes spanning from the centrum semiovale to the medulla which covered three regions of the human brain which are known to contain measurable and known iron concentrations: basal ganglia, brainstem, and cortex. DSR data were acquired using a multi-slice, multi-shot EPI (EPI factor × 9) gradient echo ($TR/TE/\alpha$ = 3000ms/5.8ms/90°) with SENSE factor = 2. RF saturation was accomplished using a 250 ms block pulse at 0.8 μT amplitude at 27 offset frequencies ranging from -750 to 750 Hz off resonance with respect to water. Nominal resolution was $1.8 \times 1.8 \times 3$ mm^3 (AP, RL, IS). A reference scan was also acquired with precisely the same sequence parameters but in the absence of RF irradiation. Only one acquisition was performed and the total scan time for multi-offset DSR imaging was 8min 30 sec. It should be noted that since the power of irradiation is low and the pulse duration is short compared to TR, the specific absorption rate (SAR) was well within allowed FDA limits (< 2 W/kg). The DSR was calculated voxel-by-voxel using Eq. 1.

Local susceptibility differences introduce a shift of the water frequency between different voxels, which can dramatically affect the magnitude of DSR and, consequently, the quality of the DSR images. Fortunately, the DSR spectrum actually contains the information needed to correct for the field inhomogeneity, and all that is needed is to artificially shift the center frequency of the DSR spectrum in each voxel to an assigned water frequency of 0 Hz. This approach of water saturation shift referencing (WASSR) can actually be used for absolute field frequency mapping, which we recently demonstrated (7). To accomplish this in a simple and convenient manner, the DSR spectrum was interpolated to 540 data points to artificially increase the spectral resolution such that the point of maximum saturation (i.e. the offset that corresponds to the 0 Hz frequency) could be determined. After interpolation, the DSR data corresponding to offset frequencies in the range of -300 to +300 Hz were retained and fitted to a 25th-order polynomial. Since the DSR at the water frequency should be maximal, the offset at which the maximum point of the fitted polynomial occurred was assigned to 0 Hz and the DSR spectrum at every voxel in the acquisition was shifted accordingly and the DSR value at the prescribed offset frequency was determined from the fitted data.

NIH-PA Author Manuscript

NIH-PA Author Manuscript

NIH-PA Author Manuscript

It should be pointed out that the use of a simplified polynomial interpolation procedure was applicable here because a relatively long RF irradiation (250ms) was used which resulted in broad DSR spectra with sufficient points to describe it. If shorter pulses were to be used, the DSR spectra would be narrower and both the offset frequency spacing and interpolation would need to be optimized accordingly (7). After shifting, the DSR values at the low frequency side of water were measured. The reason is that, even though theory predicts a symmetric DSR spectrum, we observed a slight asymmetric broadening of the high-frequency side. We hypothesize that this is a result of chemical exchange saturation transfer effects arising from solutes with exchangeable groups.

From the shift-corrected DSR images, regions of interest (ROI) were manually selected from the following brain structures: globus pallidus (GP), putamen (Put), caudate nucleus (CN), thalamus (Thal), periventricular white matter (WM), red nucleus (RN), substantia nigra (SN), and parietal cortex (Crtx). In particular, with the exception of the cortex, the ROI's were placed on each slice in which the structure of interest was visible. For the cortex, ROI's were placed in the parietal cortex on the left and right side of each of the slices in which the basal ganglia were also visible. These regions were also manually selected on the T_2*- and T_2-weighted images, and the latter was propagated to the absolute R_2 map. Because the image readout in DSR imaging caused more distortions that the conventional images, propagation from DSR to these conventional imaging types was not practical and therefore not done. The mean DSR at 120 Hz off-resonance and the mean R_2 in each of these ROI's were compared against the reported estimate of iron concentration in each structure. It is well known that some brain structures continue to accumulate iron with age, and therefore, we corrected for the age dependence of the iron concentration using the regression equations from Hallgren and Sourander (2). Finally, the contrast to noise ratios (CNR) of these metrics were compared between several neighboring structures to examine whether or not DSR contrast is sufficient at discriminating tissues from surrounding structures. The contrast to noise was defined as:

$$CNR = \left| \frac{S_a - S_b}{\sqrt{\sigma_a^2 + \sigma_b^2}} \right| \quad [9]$$

where $S_{a,b}$ are the mean signal intensities and $\sigma_{a,b}$, are the standard deviations of the mean taken from ROI's drawn in tissues a and b. After the CNR was calculated for each pair of structures in each individual, the mean and standard deviations of the CNR over all individuals was compared using Wilcoxon Rank Sum (Mann-Whitney U) Test for the existence of statistically significant differences ($p < 0.05$) between each metric.

Results

Simulations

In order to determine the experimental scan parameters, we first used the exact analytical expressions (Eqs. 3-8) to simulate the dependence of DSR on saturation power and length. An example of this at an irradiation offset frequency of 100Hz is shown in Fig. 1A. The simulation shows that effective saturation can be achieved at short saturation times when using higher power. However, short saturation pulse lengths have increased bandwidth and reduce the selectivity of the irradiation. We therefore decided to use a pulse length of 250ms. Using this setting, we then applied the full Bloch equations to simulate the power dependence of the saturation spectrum with and without MT contribution (Fig. 1B). Clearly,

NIH-PA Author Manuscript

NIH-PA Author Manuscript

NIH-PA Author Manuscript

MT effects become dramatically more dominant at higher frequency offsets and with increasing power of irradiation. As a compromise, we decided to use a power of 0.8μT where MT effects are relatively small while still having sufficient power for tissue penetration. Finally, to determine the most suitable frequency range for studying small changes in T_2 due to differences in iron content, we simulated the pure DSR curve (no MT, (8)) for T_2-values of 70 and 60ms and determined the difference spectrum (Fig. 1C). These results show a maximum difference in the offset frequency range of ±120-140Hz. As the MT contribution increases with increasing frequency, we chose to perform the *in vivo* analyses at 120Hz.

Human studies

Figure 2A shows an initial DSR (120Hz) image that we obtained in a slice through the basal ganglia. There is clear contrast in the GM nuclei, but unfortunately there is a large signal hyperintensity near the frontal lobe, similar to the one typically seen in conventional T_2* images. Upon further investigation of the voxel-by-voxel DSR spectra, we discovered that this artifact was due to a shift in the DSR spectrum that depends on the magnitude of the local magnetic susceptibility. Fortunately, and contrary to gradient-echo imaging, this problem can be addressed because we know that the center of the DSR spectrum must be at the water frequency. After correction of the susceptibility-shift on a voxel-by-voxel basis (c.f. Methods) and assigning the center to a frequency of 0Hz, we see that the correction is sufficient to display the anatomical features, as demonstrated in Fig. 2B. Finally, Fig 2C shows the magnitude of the shift (in Hz) between the true water frequency (0 Hz) and the measured DSR peak.

To test the correspondence between our simulations and experiments, we compared simulated and experimental DSR spectra for the Globus Palladus (GP) and Putamen (Put) (Fig. 2D). Measured T_2 values for GP and Put (56ms and 73ms, respectively), and reported T_1 (12) values (~1000ms and ~1300ms, respectively, Table 2) were used as input for Eqs. 3-8, together with the experimental saturation setting of $B_1 = 0.8\mu T$ and $t_{sat} = 250ms$. It can be seen that for offset frequencies below 180 Hz, simulation and experiment agree extremely well. However, at larger offset frequencies, there is a positive deflection in the experimental curve, which we attribute to MT effects, as based on the simulations in Fig. 1B. Chi-squared goodness of fit analysis of the predicted (simulated) vs. observed (experimental) data points for each curve showed that $p < 0.001$ for offsets closer to water than 180 Hz, while for offsets further away, the p-value failed to reach significance ($p = 0.2$).

Susceptibility-shift-corrected DSR (120Hz) images are shown in Figs. 3A-B for the brainstem and in Figs. 4A-C for the basal ganglia. At the level of the brainstem (Fig 3) the red nucleus (RN) and substantia nigra (SN) can be well discriminated from the surrounding tissues. Note that, due to the definition of the DSR, tissues with shorter T_2 (i.e. large R_2) will present brighter than those with longer T_2. At the level of the basal ganglia (Figs 4A-D), the GP and Put can be well appreciated from the surrounding white matter and caudate nucleus (CN). Interestingly, white matter is darker than any gray matter structure, which may reflect the fact that T_2 is not the only determinant for DSR contrast. Also, at this level and in the following panels (Figure 4B-C) the thalamus can be discriminated clearly from the white matter tracts of the posterior and retro-lenticular limbs of the internal capsule and anterior and superior thalamic radiations. Finally, in **panels A-C**, the cortical GM is quite well resolved compared to the subcortical white matter.

Figs. 3 and 4 also show corresponding absolute R_2 and T_2*-weighted images. Both image types resolve the RN, SN, and GP extremely well, but their contrast is insufficient in those tissues that contain a more subtle amount of iron, such as when CN and Put are compared to

NIH-PA Author Manuscript

NIH-PA Author Manuscript

NIH-PA Author Manuscript

the anterior limb of the internal capsule (Fig 4E-F) This result was quantitatively examined and is reflected in the CNR analysis in Table 1.

The measured DSR and R_2 values are compared with estimated, age-adjusted iron concentration and literature T_1 values in Table 2. Figure 5A shows the existence of good correlation between DSR (120Hz) and estimated, age-adjusted iron concentration ($r=0.87$, $p<0.001$). Figure 5B shows the same for R_2 ($r=0.80$, $p<0.001$). When plotting DSR(120Hz) against the observed R_2 (Fig. 5C) an excellent linear agreement ($r=0.89$, $p<0.001$) is also found.

Discussion

Origin of DSR Contrast

The results in this study show that the previously reported apparent differences in MTR contrast between different GM structures can be explained by direct saturation effects that are proportional to the iron content of these tissues. This is in line with the results from off-resonance saturation studies on superparamagnetic iron oxide particles in solution (6), where the saturation spectrum was found to broaden with increasing iron concentration. If the origin of the DSR contrast would be due solely to a reduction in T_2 with increasing iron content, this contrast would not provide any extra information over conventional T_2 and T_2*w approaches. However, when comparing DSR images with standard spin-density/T2*w acquisitions and absolute transverse relaxation rate (Figs 3 and 4) images, some interesting features become apparent. For instance, except for the globus pallidus, substantia nigra and red nucleus (which are known to house the highest iron concentration in the human brain) and perhaps the posterior aspect of the thalamus, the gray matter regions in the basal ganglia (Fig. 4) are not well distinguished from surrounding tissues in the spin-density/T_2*w (Figs. 4D-F) and R_2 (Figs. 4G-I) images. The R_2 images also display little contrast between white and gray matter, which is not unexpected, as the spin density contribution has been removed in these absolute relaxation images and the T_2 is not very different between these two tissues. It should also be noted that even though T_2 is slightly longer for cortex than for WM in Table 2, which may be due to partial volume effects from CSF. In some parts of the brain, cortex is known to have a T_2 lower than WM, which has also been attributed to ferritin presence (17-19). The DSR images also lack a spin density contribution, as this is divided out in calculation of the ratio of signals with and without RF irradiation. Interestingly, however, DSR images still show clear contrast between all GM and WM regions. When studying Eqs. [4-8], the only plausible explanation for this apparent difference is a contribution fromT_1. This is not surprising in view of the well-known correspondence between T_1 and water content (20). Because of the increased water content (0.82 ml/g vs. 0.72 ml/g) of GM vs. WM (21), the T_1 of GM is longer than that of WM (Table 2), making all GM regions clearly visible in DSR images. Thus, DSR imaging provides a combined T_1 and T_2 contrast, with a somewhat complex interplay between the proportional contributions of both relaxation mechanisms and the offset frequency used for irradiation. While this appears to be a nuisance at first, it may actually provide greater utility for certain applications, such as the study of subtle changes in paramagnetic components of tissue in diseased populations, or for tracking paramagnetically labeled cells with a concentration of agent optimized for detection by DSR.

It should be made transparent that DSR imaging is not simply specific for iron imaging, but rather for any changes in T_2. This is powerful in that it will allow the study of many diseases and can even be applied to fMRI. Actually, the effect of off-resonance saturation on BOLD contrast has been a topic of discussion (22,23) and we have recently shown that DSR imaging can be used for detection of functional MRI activation (24).

NIH-PA Author Manuscript

NIH-PA Author Manuscript

NIH-PA Author Manuscript

Experimental Considerations

These first DSR data presented here are based on reasonably optimized parameters allowing direct water saturation to be measured at an offset frequency where there is little influence from MT effects. The approach can be further improved by the use of shorter saturation pulses, as these will produce sharper saturation curves that will be more sensitive to relaxation time changes. It is important to realize, however, that such a narrowing will provide improvement until the point that the bandwidth of RF irradiation becomes too large and the specificity for saturation at a particular frequency is lost. It should also be pointed out that when reducing the saturation time, the spin system might no longer be in steady state, which complicates the theoretical interpretation (8). Nevertheless, the steady state criterion depends on the complete set of experimental parameters. For example, when performing a multi-slice experiment in which saturation is applied before each slice, the brain tissue water will quickly reach steady state if TR is sufficiently short. Another problem with reducing the width of the saturation spectrum is that it becomes necessary to acquire more points to be able to properly sample the DSR curves for all brain regions as these curves will need to be shifted around based on local susceptibility differences. Guidelines for setting the sweep width and the number of points for such acquisitions were recently presented in the WASSR approach for mapping the absolute water frequency using direct water saturation (7). These guidelines can be used to optimize the duration of the experiment, which is mainly determined by both the image resolution and the spectral resolution of the DSR curves. In the current study, we heavily oversampled the DSR spectra to be able to determine 1) the magnitude of the susceptibility-related frequency shift, and 2) which offsets would be optimally sensitive to line broadening. Based on the guidelines in the WASSR paper (7), it is reasonable to acquire about 16-32 points over a sweep width that is about three-four times the linewidth of the DSR spectrum. Because TR does not affect the shape of the curve, it could be further shortened and thus allow for whole brain coverage in a very reasonable scan time (one to a few minutes), depending on the power deposition at a given field strength.

One apparent benefit of DSR imaging over T_2*-weighted and other susceptibility weighted imaging (SWI) approaches (25,26) is that DSR imaging affords the ability to correct for local susceptibility shifts by using the information contained in the DSR spectrum to extract the water frequency center. This should allow one to use DSR to image regions of the human body where these conventional approaches are difficult, such as the liver, muscles, and heart. In the current paper we used a simple algorithm for fitting the DSR spectra, as we had sufficient points sampled for describing the DSR curves. A more sophisticated approach for optimum sampling followed by centering and symmetrizing saturation spectra was recently presented (WASSR, (7)), which would further enhance the application of DSR in difficult regions in the human body.

Terminology

Finally, to avoid confusion, it is important to discuss terminology. Off-resonance saturation (ORS) reduces the observed water signal through both magnetization transfer (MT) and direct saturation (DS) effects. MT effects are due to either saturation of semisolid tissue protons followed by dipolar transfer or chemical exchange from these protons to the surrounding water protons (conventional MT contrast or MTC) or the chemical exchange saturation transfer (CEST, (7,27,28)) effect in which exchangeable protons are saturated, followed by exchange transfer to water. ORS induces a convolution of MTC, CEST, and DS effects, the proportional contribution of which depends on the irradiation frequency offset ($\Delta\omega$), power (B_1), and duration (t_{sat}). While MTC and CEST effects are known to be asymmetric with respect to the water frequency (29,30), Direct saturation leads to a symmetric Lorentzian lineshape that can be described by an exact analytical solution of the

NIH-PA Author Manuscript

NIH-PA Author Manuscript

NIH-PA Author Manuscript

Bloch equations (8) and by a line width proportional to T_2, not T_2*. The current paper is focused on the study of DS effects, which have previously been seen only as a nuisance when trying to interpret MTC and CEST phenomena. Direct water saturation can be selectively measured by using ORS pulses that are of sufficiently low power and short duration to avoid most MT effects. It is now becoming clear that DS imaging may have several applications, one being the imaging of line shape changes due to increases or decreases in T_2 or T_1, and another, the mapping of absolute water frequencies for either CEST image corrections of field mapping (WASSR, (7)). Changes in T_2 can be due to line broadening, such as in the case of diffusion through field gradients caused by presence of paramagnetic substances (6), or line narrowing, such as during functional activation (24). We expect to find more applications of direct water saturation imaging in the future.

Conclusion

We explored the use of direct saturation ratio (DSR) imaging for sensitizing MRI to differences in iron content between gray matter brain structures. DSR MRI clearly outlined gray matter regions (hyperintense) with respect to white matter. In addition, gray matter contrast was found to be proportional to iron content known for these structures from the literature. This contrast was a result of the dependence of the direct saturation ratio (DSR) on both paramagnetic T_2 shortening due to the presence of iron and a longer T_1 with respect to white matter. On the contrary, conventional absolute T_2 MRI could not outline the cortex, while different GM regions in T_2*w imaging could have either lower or higher intensity than WM. These first direct saturation measurements *in vivo* provide a new opportunity to study tissue properties. When experimental parameters are optimized so that magnetization transfer effects are negligible, DSR imaging is a quantitative method with a well-defined theoretical analytical interpretation (Eqs. 2-8). As such, we hypothesize that it has potential for longitudinal monitoring of tissue changes resulting from conditions such as simple aging, Alzheimer's disease, Huntington's disease, and hemochromatosis. More studies will need to be performed to find out whether DSR imaging will have the sensitivity and specificity for assessing patient populations.

Acknowledgments

This publication was made possible by Grant Number P41 RR015241 from the National Center for Research Resources (NCRR), a component of the National Institutes of Health (NIH). Its contents are solely the responsibility of the authors and do not necessarily represent the official view of NCRR or NIH. The authors would like to thank Dr. Jared Parker for his conversations on experimental design; Ms. Terri Brawner, Ms. Kathleen Kahl, and Ms. Ivana Kusevic for their assistance with data acquisition; Dr. Assaf Gilad for his insight and useful discussions on paramagnetic relaxation. Dr. Peter van Zijl is a paid lecturer for Philips Medical Systems. Dr. van Zijl is the inventor of technology that is licensed to Philips. This arrangement has been approved by The Johns Hopkins University in accordance with its Conflict of Interest policies.

Grant Support: NIH/NCRR (RR015241)

References

1. Smith SA, Farrell JA, Jones CK, Reich DS, Calabresi PA, van Zijl PC. Pulsed magnetization transfer imaging with body coil transmission at 3 Tesla: feasibility and application. Magn Reson Med. 2006; 56(4):866–875. [PubMed: 16964602]
2. Hallgren B, Sourander P. The effect of age on the non-haemin iron in the human brain. J Neurochem. 1958; 3(1):41–51. [PubMed: 13611557]
3. Elster AD, King JC, Mathews VP, Hamilton CA. Cranial tissues: appearance at gadolinium-enhanced and nonenhanced MR imaging with magnetization transfer contrast. Radiology. 1994; 190(2):541–546. [PubMed: 8284413]

NIH-PA Author Manuscript

NIH-PA Author Manuscript

NIH-PA Author Manuscript

4. Papanikolaou N, Ghiatas A, Kattamis A, Ladis C, Kritikos N, Kattamis C. Non-invasive myocardial iron assessment in thalassaemic patients. T2 relaxometry and magnetization transfer ratio measurements. Acta Radiol. 2000; 41(4):348–351. [PubMed: 10937756]
5. Salustri C. Lack of magnetization transfer from the ferritin molecule. J Magn Reson B. 1996; 111(2):171–173. [PubMed: 8661275]
6. Zurkiya O, Hu X. Off-resonance saturation as a means of generating contrast with superparamagnetic nanoparticles. Magn Reson Med. 2006; 56(4):726–732. [PubMed: 16941618]
7. Kim M, Gillen JS, Landman BA, Zhou J, van Zijl PCM. Magn Reson Med. 2008 In Press.
8. Mulkern RV, Williams ML. The general solution to the Bloch equation with constant rf and relaxation terms: application to saturation and slice selection. Med Phys. 1993; 20(1):5–13. [PubMed: 8455512]
9. Bryant RG. The dynamics of water-protein interactions. Annu Rev Biophys Biomol Struct. 1996; 25:29–53. [PubMed: 8800463]
10. Henkelman RM, Huang X, Xiang QS, Stanisz GJ, Swanson SD, Bronskill MJ. Quantitative interpretation of magnetization transfer. Magn Reson Med. 1993; 29(6):759–766. [PubMed: 8350718]
11. Wolff SD, Balaban RS. Magnetization transfer contrast (MTC) and tissue water proton relaxation in vivo. Magn Reson Med. 1989; 10(1):135–144. [PubMed: 2547135]
12. Gelman N, Ewing JR, Gorell JM, Spickler EM, Solomon EG. Interregional variation of longitudinal relaxation rates in human brain at 3.0 T: relation to estimated iron and water contents. Magn Reson Med. 2001; 45(1):71–79. [PubMed: 11146488]
13. Lu H, Clingman C, Golay X, van Zijl PC. Determining the longitudinal relaxation time (T1) of blood at 3.0 Tesla. Magn Reson Med. 2004; 52(3):679–682. [PubMed: 15334591]
14. Sled JG, Pike GB. Quantitative interpretation of magnetization transfer in spoiled gradient echo MRI sequences. J Magn Reson. 2000; 145(1):24–36. [PubMed: 10873494]
15. Stanisz GJ, Odrobina EE, Pun J, Escaravage M, Graham SJ, Bronskill MJ, Henkelman RM. T1, T2 relaxation and magnetization transfer in tissue at 3T. Magn Reson Med. 2005; 54(3):507–512. [PubMed: 16086319]
16. Hermier M, Nighoghossian N. Contribution of susceptibility-weighted imaging to acute stroke assessment. Stroke. 2004; 35(8):1989–1994. [PubMed: 15192245]
17. Bartha R, Michaeli S, Merkle H, Adriany G, Andersen P, Chen W, Ugurbil K, Garwood M. In vivo 1H2O T2+ measurement in the human occipital lobe at 4T and 7T by Carr-Purcell MRI: detection of microscopic susceptibility contrast. Magn Reson Med. 2002; 47(4):742–750. [PubMed: 11948736]
18. Georgiades CS, Itoh R, Golay X, van Zijl PC, Melhem ER. MR imaging of the human brain at 1.5 T: regional variations in transverse relaxation rates in the cerebral cortex. AJNR Am J Neuroradiol. 2001; 22(9):1732–1737. [PubMed: 11673169]
19. Zhou J, Golay X, van Zijl PC, Silvennoinen MJ, Kauppinen R, Pekar J, Kraut M. Inverse T(2) contrast at 1.5 Tesla between gray matter and white matter in the occipital lobe of normal adult human brain. Magn Reson Med. 2001; 46(2):401–406. [PubMed: 11477646]
20. Lin W, Paczynski RP, Venkatesan R, He YY, Powers WJ, Hsu CY, Haacke EM. Quantitative regional brain water measurement with magnetic resonance imaging in a focal ischemia model. Magn Reson Med. 1997; 38(2):303–310. [PubMed: 9256112]
21. Gelman N, Gorell JM, Barker PB, Savage RM, Spickler EM, Windham JP, Knight RA. MR imaging of human brain at 3.0 T: preliminary report on transverse relaxation rates and relation to estimated iron content. Radiology. 1999; 210(3):759–767. [PubMed: 10207479]
22. Song AW, Wolff SD, Balaban RS, Jezzard P. The effect of off-resonance radiofrequency pulse saturation on fMRI contrast. NMR Biomed. 1997; 10(4-5):208–215. [PubMed: 9430350]
23. Zhou J, Payen JF, van Zijl PC. The interaction between magnetization transfer and blood-oxygen-level-dependent effects. Magn Reson Med. 2005; 53(2):356–366. [PubMed: 15678541]
24. Donahue, M.; Hua, J.; Edden, R.; Smith, S.; van Zijl, P. Detecting Brain Activity Using Direct Water Saturation. Toronto: 2008 April. p. 402
25. Haacke EM, Xu Y, Cheng YC, Reichenbach JR. Susceptibility weighted imaging (SWI). Magn Reson Med. 2004; 52(3):612–618. [PubMed: 15334582]

NIH-PA Author Manuscript

NIH-PA Author Manuscript

NIH-PA Author Manuscript

26. Schenck JF. Magnetic resonance imaging of brain iron. J Neurol Sci. 2003; 207(1-2):99–102. [PubMed: 12614939]

27. Sherry AD, Woods M. Chemical exchange saturation transfer contrast agents for magnetic resonance imaging. Annu Rev Biomed Eng. 2008; 10:391–411. [PubMed: 18647117]

28. Zhou J, Wilson DA, Sun PZ, Klaus JA, Van Zijl PC. Quantitative description of proton exchange processes between water and endogenous and exogenous agents for WEX, CEST, and APT experiments. Magn Reson Med. 2004; 51(5):945–952. [PubMed: 15122676]

29. Hua J, Jones CK, Blakeley J, Smith SA, van Zijl PC, Zhou J. Quantitative description of the asymmetry in magnetization transfer effects around the water resonance in the human brain. Magn Reson Med. 2007; 58(4):786–793. [PubMed: 17899597]

30. Pekar J, Jezzard P, Roberts DA, Leigh JS Jr, Frank JA, McLaughlin AC. Perfusion imaging with compensation for asymmetric magnetization transfer effects. Magn Reson Med. 1996; 35(1):70–79. [PubMed: 8771024]

31. Chen, L.; Bernstein, MA.; Huston, J.; Fain, S. Measurements of T1 relaxation times at 3.0T: implications for clinical MRA. Glasgow: 2001. p. 1391

32. Lu H, Nagae-Poetscher LM, Golay X, Lin D, Pomper M, van Zijl PC. Routine clinical brain MRI sequences for use at 3.0 Tesla. J Magn Reson Imaging. 2005; 22(1):13–22. [PubMed: 15971174]

NIH-PA Author Manuscript
NIH-PA Author Manuscript
NIH-PA Author Manuscript

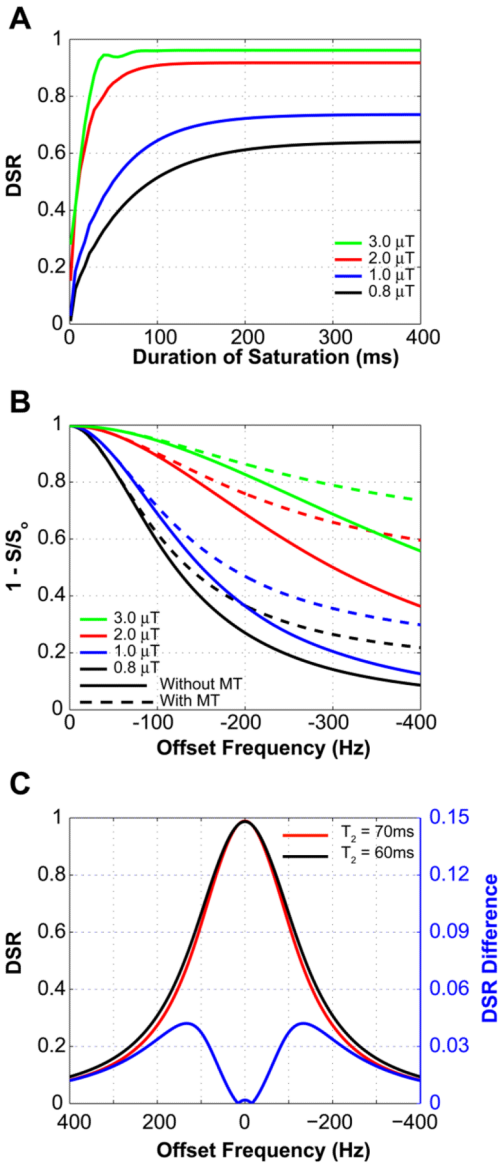

Figure 1.

A) Effect of duration and power of RF irradiation on the DSR signal intensity for gray matter (T_2 = 70ms; T_1 = 1100ms; offset = 100Hz; Eqns. 3-8). Short duration and high power provides rapid saturation, but longer pulses with much less power achieve saturation in approximately 200 ms. B) saturation spectra with (dotted line) and without (solid line) MT effect as a function of offset frequency for 4 saturation pulse amplitudes at t_{sat} = 250ms (simulation using full Bloch Equations). For this pulse duration, at higher power and greater offset frequencies, the MT effect starts to contribute substantially to signal intensity. C) DSR change for a 15% decrease in T_2, (Eqs. 3-8; B_1 = 0.8μT and t_{sat} = 250 ms). The offset corresponding to the greatest DSR difference is in the range of 120 – 140 Hz.

NIH-PA Author Manuscript

NIH-PA Author Manuscript

NIH-PA Author Manuscript

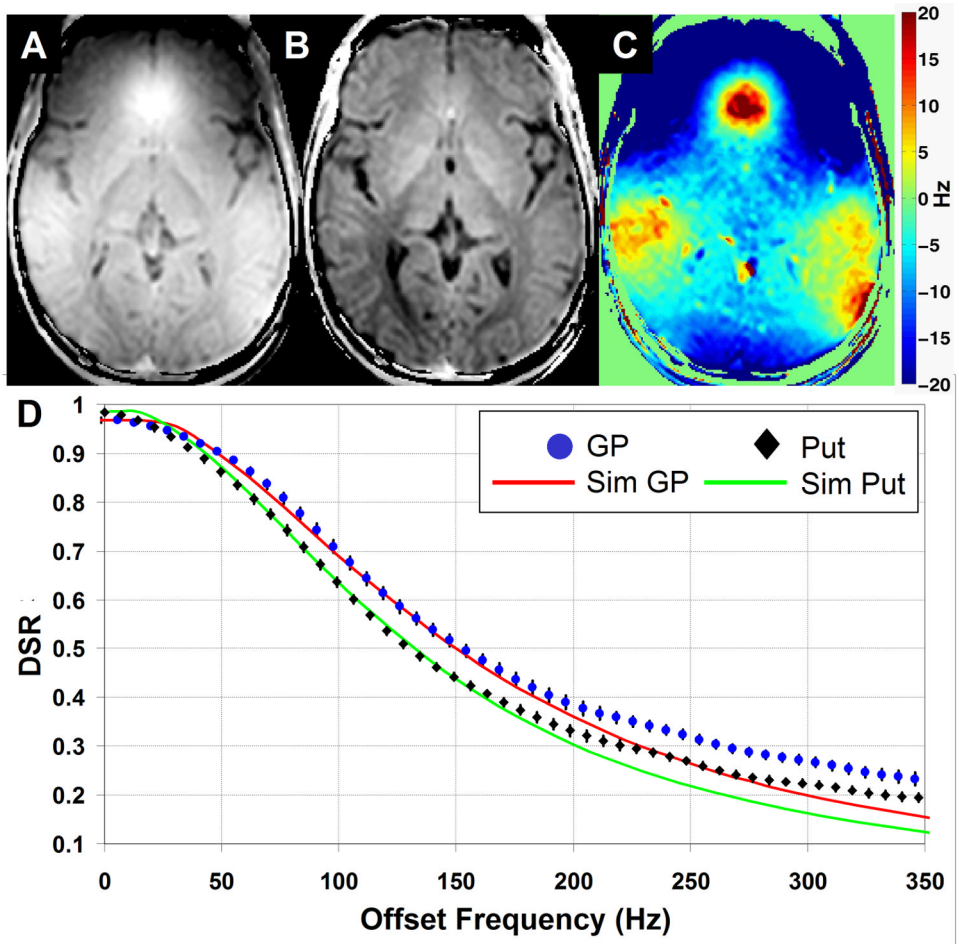

Figure 2.

DSR(120Hz) images before (A) and after (B) susceptibility-shift correction. C) Map of the magnitude of the susceptibility shift (in Hz). The post-correction image reveals excellent discrimination between all of the GM structures and between gray and white matter. D) Comparison of experimental and theoretical DSR spectra from two regions of interest: Globus Pallidus (circle) and Putamen (diamond). The analytical solution (Eqs. 3-8) was used for the simulation with RF amplitude = 0.8μT, t_{sat} = 250ms, and T_1/T_2 values of 1000ms/56ms and 1300ms/73ms, respectively. χ^2 ($p < 0.001$) analysis shows that for offsets < 180 Hz, simulation and experiment agree significantly, while for offsets > 180 Hz, there is substantial deviation due to the presence of MT effects

NIH-PA Author Manuscript

NIH-PA Author Manuscript

NIH-PA Author Manuscript

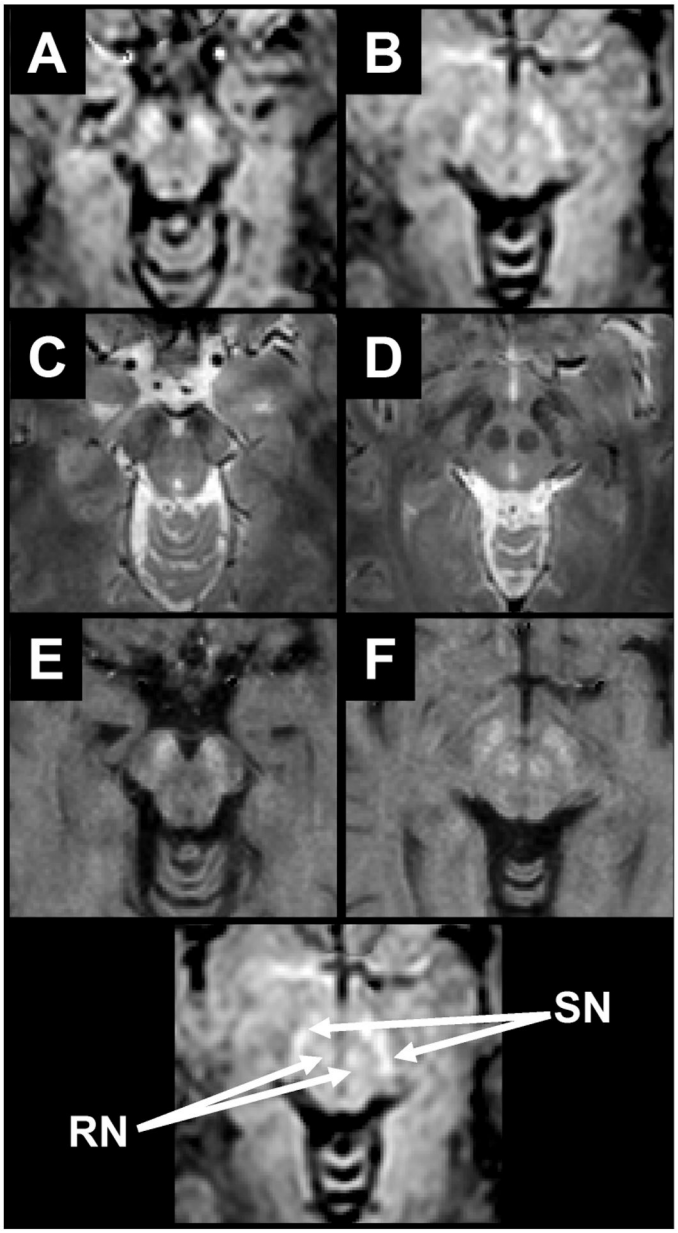

Figure 3.
Comparison of DSR (A-B), T_2*-weighted (C-D), and absolute R_2 (E-F) images. A location key is given at the bottom. For DSR, the contrast is similar to R_2 in that regions of high iron concentration exhibit increased intensity. At the level of the brain stem the SN and RN can be seen in all three image types.

NIH-PA Author Manuscript

NIH-PA Author Manuscript

NIH-PA Author Manuscript

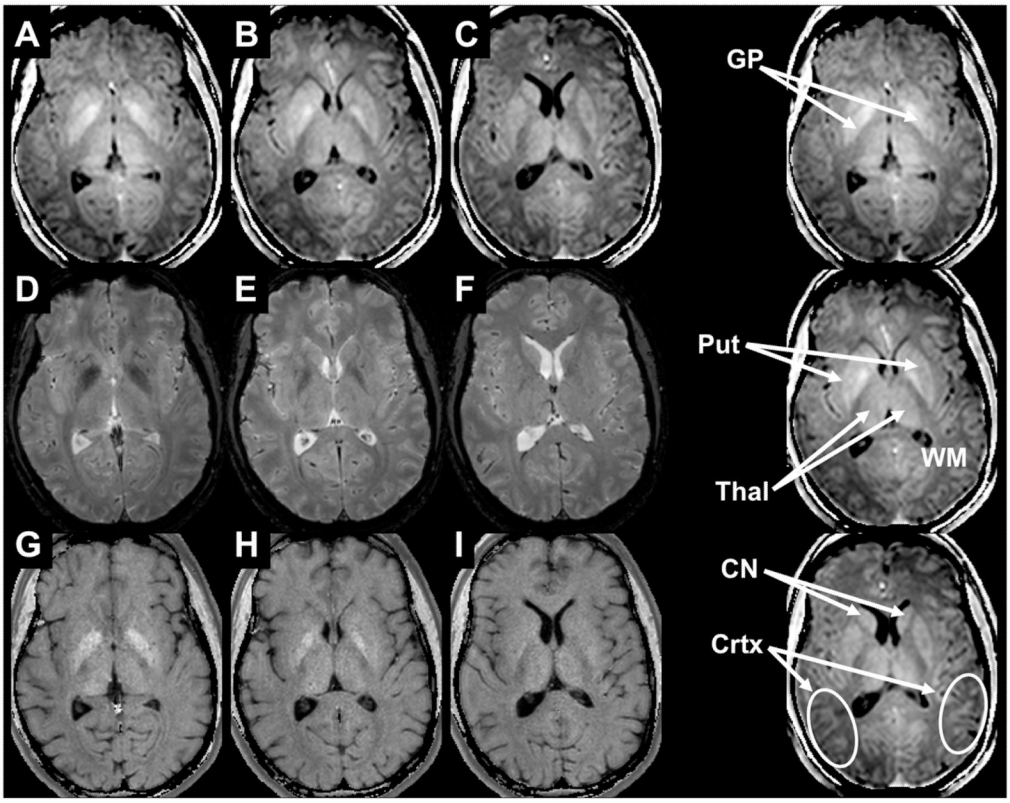

Figure 4.
Comparison of DSR (A-C), T_2*w (D-F), and absolute R_2 (G-I) images at the level of the basal ganglia. The GP is well seen on the first two panels for all modalities. The DSR separates the different GM structures as for instance the CN in Panels C, F, and I.

NIH-PA Author Manuscript

NIH-PA Author Manuscript

NIH-PA Author Manuscript

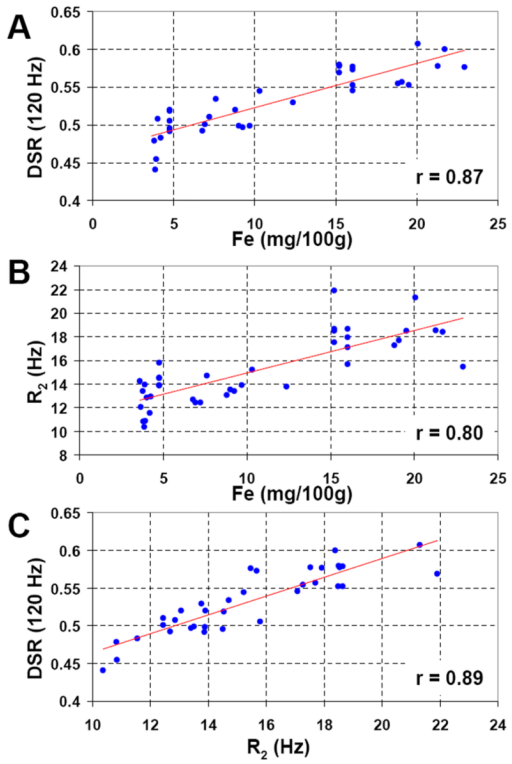

Figure 5.

Regression analyses. A) Plot of the mean DSR(120 Hz) in ROI's drawn in each individual and in each structure listed in the methods vs. the age adjusted iron concentration reported for these same structures. Linear regression shows a strong association ($r = 0.87$, $p < 0.001$) suggesting the ability for DSR to detect differences in iron concentration *in vivo*. B) Previously it has been often reported that that R_2 linearly increases with increasing iron concentration and in (B) a similar regression analysis with R_2 and age adjusted iron concentration confirms this ($r = 0.80$, $p < 0.01$). C) To test the strength of the expected relationship between DSR and R_2, a similar regression reveals a strong association ($r = 0.89$, $p < 0.001$).

NIH-PA Author Manuscript
NIH-PA Author Manuscript
NIH-PA Author Manuscript

Table 1

Contrast to Noise Ratio between different structures for R_2, DSR(120 Hz), and T_2*-weighted images

	GP:Put	GP:CN	Put:CN	RN:SN	Crtx:WM	Thal:WM	Put:WM	GP:WM
DSR	***4.2 ± 0.6***†§	***4.2 ± 0.6***	0.8 ± 0.3	***1.5 ± 0.9***	***3.6 ± 2.3***	***6.8 ± 2.5***†	***7.8 ± 3.2***†§	***9.9 ± 0.8***†§
R2	2.7 ± 0.2	3.4 ± 0.4	0.8 ± 0.3	1.1 ± 0.6	2.1 ± 1.2	1.2 ± 0.9	0.9 ± 0.4	3.2 ± 0.6
T2*w	2.6 ± 0.4	3.9 ± 0.1	0.5 ± 0.1	1.1 ± 0.6	3.4 ± 0.5	3.2 ± 1.5	1.3 ± 0.2	2.2 ± 0.5

Mean ± SD over all individuals; Maximum CNR value for the column is in bold + italic. † and § indicate results from Wilcoxon Rank Sum tests for statistical differences ($p < 0.05$):

†DSR different from R_2,

§DSR different from T_2*w,

NIH-PA Author Manuscript

NIH-PA Author Manuscript

NIH-PA Author Manuscript

Table 2

Comparison of estimated age-adjusted iron concentration, measured T_2, measured DSR, and literature T_1 range for several GM and WM structures in the brain.

Structure	Fe (mg/100g)*	T_2 (ms)	DSR	T_1 (ms)†
GP	21.3 ± 3.5	53.6 ± 4.5	0.57 ± 0.02	1043 ± 37
RN	19.5 ± 6.9	59.0 ± 4.8	0.56 ± 0.01	N/A
SN	18.5 ± 6.5	52.7 ± 4.7	0.58 ± 0.01	1147 ± 50
Put	13.3 ± 3.4	71.7 ± 3.7	0.51 ± 0.22	1102 - 1337
CN	9.3 ± 2.1	76.6 ± 5.6	0.51 ± 0.03	1258 - 1483
Thal	4.8 ± 1.2	68.9 ± 3.7	0.50 ± 0.01	986 - 1218
Crtx	3.8 ± 0.7	88.6 ± 7.6	0.47 ± 0.3	1280 - 1763
WM	4.2 ± 0.9	75.2 ± 4.9	0.43 ± 0.01	791 - 847

Mean ± SD over all individuals

*calculated from (2)

†(12,31,32)

N/A: Not available